Dynamic connectivity modulates local activity in the core regions of the default-mode network

Wei Tang[a,1,2], Hesheng Liu[a,2], Linda Douw[a,b], Mark A. Kramer[c], Uri T. Eden[c], Matti S. Hämäläinen[a], and Steven M. Stufflebeam[a]

[a]Athinoula A. Martinos Center for Biomedical Imaging, Massachusetts General Hospital/Harvard Medical School, Charlestown, MA 02129; [b]Department of Anatomy and Neurosciences, VU University Medical Center, 1081 HV Amsterdam, The Netherlands; and [c]Department of Mathematics and Statistics, Boston University, Boston, MA 02215

Edited by Marcus E. Raichle, Washington University in St. Louis, St. Louis, MO, and approved July 28, 2017 (received for review February 6, 2017)

Segregation and integration are distinctive features of large-scale brain activity. Although neuroimaging studies have been unraveling their neural correlates, how integration takes place over segregated modules remains elusive. Central to this problem is the mechanism by which a brain region adjusts its activity according to the influence it receives from other regions. In this study, we explore how dynamic connectivity between two regions affects the neural activity within a participating region. Combining functional magnetic resonance imaging (fMRI) and magnetoencephalography (MEG) in the same group of subjects, we analyzed resting-state data from the core of the default-mode network. We observed directed influence from the posterior cingulate cortex (PCC) to the anterior cingulate cortex (ACC) in the 10-Hz range. This time-varying influence was associated with the power alteration in the ACC: strong influence corresponded with a decrease of power around 13–16 Hz and an increase of power in the lower (1–7 Hz) and higher (30–55 Hz) ends of the spectrum. We also found that the amplitude of the 30- to 55-Hz activity was coupled to the phase of the 3- to 4-Hz activity in the ACC. These results characterized the local spectral changes associated with network interactions. The specific spectral information both highlights the functional roles of PCC–ACC connectivity in the resting state and provides insights into the dynamic relationship between local activity and coupling dynamics of a network.

default-mode network | resting state | fMRI | MEG | functional connectivity

A fundamental feature of large-scale human brain activity is concurrent segregation and integration (1–4). Different brain regions can be activated by subcomponents of a cognitive process, forming distributed neural representations. These segregated regions interact with each other through network connectivity, leading to an integrated outcome that determines behavior. This dual feature sets two major paradigms in cognitive neuroimaging (3, 5–8): one investigates the localized activity that represents cognitive subprocesses; the other investigates the cross-regional coupling that reflects integration across functional modules.

While the neuroimaging field advances on both topics, gaps remain between findings. The biological basis of the integration across segregated modules remains poorly understood. Central to this question is the mechanism by which one region adjusts its local activity under the influence of other regions, a necessary step for the network to reach a downstream output. However, existing literature has focused on either localized activity or cross-region connectivity, but rarely the relationship between the two.

The difficulty lies in studying connectivity and local activity at the same time. Such an approach would require data with high spatial and temporal resolution, which is difficult to achieve with current imaging techniques (5, 9, 10). Recently, many in the field have attempted to bridge these gaps. One approach is to put sliding windows on functional magnetic resonance imaging (fMRI) data, adding temporal information to the spatial patterns of connectivity (for a review of the methods, see, for example, ref. 11, but also see ref. 12). Another approach is to compare magnetoencephalography (MEG)-based connectivity with those measured from fMRI, verifying the identities of dynamically interacting regions (10, 13–17). These new methods retrieve the spatial and temporal information of a network, making it possible to study correspondent changes in both connectivity and local activity.

Here, we investigate the relationship between cross-region connectivity and within-region activity in the default-mode network (DMN). We chose the DMN for two reasons. First, the DMN is known to activate in the resting state (18, 19), and resting state avoids the mixture of network- and stimulus-driven activity. Second and most important, the DMN is an excellent candidate for studying ongoing cognition (19, 20). Its resting-state activity is closely associated with higher functions such as autobiographic memory and self-referential thoughts. Therefore, the biological meaning of the activity–connectivity association in the DMN is within the context of cognitive processing, regardless of the absence of a task.

We recorded fMRI and MEG data in the same group of subjects and focused the analysis on two core regions of the DMN (19, 20): the anterior and the posterior cingulate cortex (ACC and PCC, respectively). We quantified short-time Granger causality (GC) between the ACC and PCC in the MEG source space under the guidance of fMRI. This dynamic measure allowed us to examine within-region spectral changes of neural activity, and at the same time, how they correspond to the change of cross-region connectivity.

Significance

When a person is at wakeful rest, not paying particular attention to the environment, his/her brain activity will not drift into random noise. Instead, it maintains robust dynamical structures to support ongoing cognition. Previous studies on the resting state have focused on either connectivity features across brain regions or local activity features within regions. Here, we show that the interactions between regions are dynamic and covary with local activity. This covariation provides insights into the neural underpinnings of ongoing cognition that is driven by the brain's intrinsic network interactions.

Author contributions: W.T., H.L., M.S.H., and S.M.S. designed research; W.T. and H.L. performed research; H.L., M.A.K., and U.T.E. contributed new reagents/analytic tools; W.T. and L.D. analyzed data; and W.T., H.L., M.A.K., M.S.H., and S.M.S. wrote the paper.

The authors declare no conflict of interest.

This article is a PNAS Direct Submission.

[1]Present address: Division of Basic Neuroscience, McLean Hospital, Belmont, MA 02478.

[2]To whom correspondence may be addressed. Email: wtang6@mclean.harvard.edu or hesheng@nmr.mgh.harvard.edu.

This article contains supporting information online at www.pnas.org/lookup/suppl/doi:10.1073/pnas.1702027114/-/DCSupplemental.

NEUROSCIENCE

The results characterized how interactions between brain regions affect the within-region activity in a real-time manner. In particular, we found that the influence from the PCC in one frequency band was associated with local spectral changes in the ACC in multiple frequency bands. Moreover, the local frequency bands held a phase–amplitude relationship that reveals the possible functional consequence of the PCC–ACC interactions.

Results

We first verified that GC reliably captured the ACC–PCC connectivity in the MEG source space. The procedure consisted of two steps: (*i*) we used functional-connectivity MRI (fcMRI) as a guide to locate the MEG frequency range that contributed the most to the ACC–PCC connectivity; (*ii*) we used that frequency range to compute seed-based GC maps, which independently replicated the connectivity pattern between the ACC and PCC.

Next, we investigated whether the temporal change of GC was associated with a local power alteration of the MEG source signal. We compared the power spectral density (PSD) between the time periods when GC to a region was strong and when GC was weak. For the frequency components of the source signal that showed a PSD difference, we also tested for cross-frequency coupling to see whether the modulated activity carried functionally meaningful structures.

The 10-Hz Neural Activity as a Major Contributor to the fMRI-Based Connectivity. We computed the temporal correlations of power between MEG sources in the ACC and PCC as a measure of overall MEG connectivity across time. The source signals were first orthogonalized to remove spurious zero-lag correlation caused by crosstalk (refs. 10 and 15, and *Materials and Methods*). Narrow-band power envelopes were then extracted from the ACC and PCC sources to compute cross-region correlations for different frequency combinations between 1 and 56 Hz. The strongest correlation was found with the 10-Hz power envelopes (Fig. 1*A*), which survived the permutation test (*Materials and Methods*).

We also computed fcMRI between the ACC and PCC using the blood oxygenation level-dependent (BOLD) signal. The 10-Hz power envelope connectivity and fMRI connectivity showed a significant cross-subject correlation (Pearson's $r = 0.39$, $P < 0.04$, Fig. 1*B*), suggesting that individuals with stronger fcMRI also have stronger MEG connectivity at 10 Hz. Thus, we consider the 10-Hz-range neural activity to be a major contributor to the functional connectivity between the ACC and PCC.

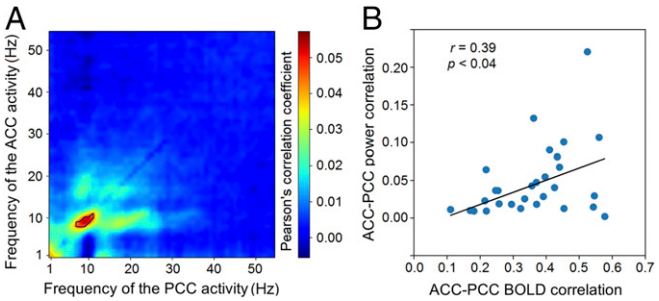

Fig. 1. MEG connectivity around 10 Hz is associated with fMRI-based connectivity. (*A*) Heatmap of the temporal correlation between the leakage-corrected power envelopes of MEG sources in the ACC and PCC. Color represents the mean Pearson's *r* scores across subjects at each frequency pair. The black line marks significant *r* scores within the contour that passed the permutation test. (*B*) Scatter plot of the MEG connectivity around 10 Hz against the fcMRI. Each dot represents a subject, and the regression line is shown in black.

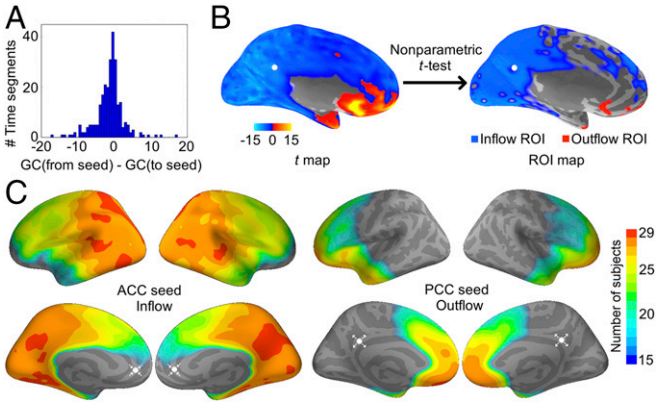

Fig. 2. Seed-based maps of GC-flow in the 10-Hz range. (*A*) Histogram from one subject as an example of the GC-flow between the seed and an arbitrary vertex over the interheartbeat time segments. The mean centered at zero, indicating no GC-flow in either direction. (*B*) Example from one subject illustrating the significance test for the GC-flow of a PCC seed. Positive *t* scores indicate outflow, and negative *t* scores, inflow. (*C*) Group-level estimation of the significant inflow to the ACC (*Left*) and outflow from the PCC (*Right*). Cross-subject conjunction scores are shown in color. Scores below 15 (i.e., consistency of less than one-half of the subjects) are not displayed. White dots indicate the seed locations, and arrows, the flow direction.

Spatially Specific GC Between the ACC and PCC in the Seed-Based Maps. Since the highest cross-subject correlation was found with activity near 10 Hz, we computed GC in the 10-Hz range for each interheartbeat time segment, as a sliding-window type of measurement for the dynamic MEG connectivity. Before testing the association between connectivity and local activity, we checked the spatial specificity of the GC measurement. This step was both to verify that GC effectively captured the connectivity, and to rule out a potential bias due to preselection of the ACC and PCC regions in the previous analysis. To do so, we used seed-based maps: when one region was set as seed, the GC measurement should show large clustered values around the other region and random small values in the rest of the cortex.

Due to technical concerns (*Discussion*), we used the difference score between the from-seed and to-seed GC (Fig. 2*A*) instead of the raw GC value. Positive scores were marked as "outflow" and negative scores "inflow." A nonparametric cluster-level test was performed across time segments to determine the significance of GC-flow at each vertex (*Materials and Methods*). Significant vertices were marked as regions of interest (ROIs), representing regions of large GC-flow values (Fig. 2*B*). ROIs were first drawn in each subject and then overlaid across subjects to derive a group-level estimation (Fig. 2*C*). For the inflow to the ACC seed, the PCC appeared to be an ROI that sent out GC influence in all 29 subjects. For the outflow from the PCC seed, the ACC appeared to be an ROI that received GC influence in 28 subjects. We did not find a PCC ROI in the ACC outflow map or an ACC ROI in the PCC inflow map (Figs. S1 and S2). The results consistently showed that the GC influence was specifically directed from the PCC to the ACC.

GC-Associated Power Spectral Changes Within the ACC. The seed-based GC maps not only verified the spatial specificity of the ACC–PCC interactions but also suggested directional asymmetry. Since stronger GC was directed from the PCC to the ACC than vice versa, we examined how local activity in the ACC changes according to GC influence from the PCC. Specifically, we measured the intensity of PSD in the ACC under different GC strengths. GC and PSD were estimated at each vertex of the ACC for each interheartbeat time segment (Fig. 3*A*). We grouped the vertices and time segments into spatiotemporal clusters

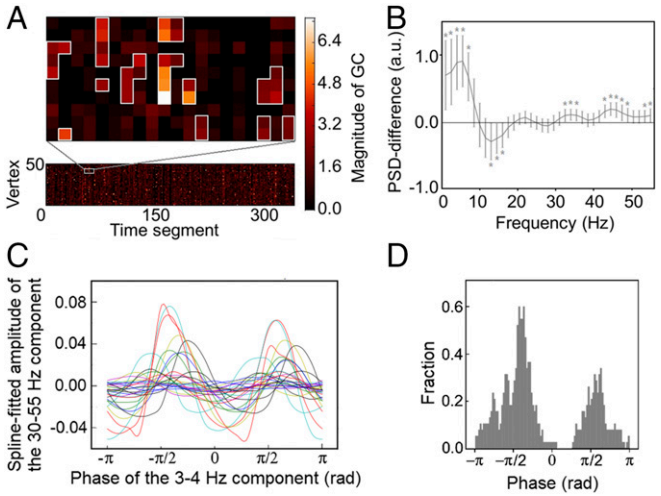

Fig. 3. Systematic local activity changes associated with the 10-Hz GC fluctuation. (*A*) Example from one subject showing the spatiotemporal GC clusters within the ACC. The lower plot shows the alpha-band GC from the PCC to each vertex in the ACC across time segments. The plot above is a magnified view showing the spatiotemporal clusters from the chosen part of the lower plot. The vertices are arranged such that those in the clusters are spatially consecutive in the cortical surface. (*B*) Power difference of the activity inside and outside the clusters, shown as mean ± SEM across subjects. Asterisks denote the significant deviation from zero (*$P < 0.05$, Bonferroni corrected for 37 comparisons; Table S1). (*C*) Spline-fitted gamma amplitude over the 3- to 4-Hz phase in the ACC showing peaks around $\pm\pi/2$. Each line represents one subject. (*D*) Histogram of the phase angles whose corresponding gamma amplitudes ranked in the top 5%. All subjects were pooled together. The count was standardized by dividing the total counts.

according to their GC values (*Materials and Methods*). A cluster represented a spatiotemporal pattern that was stable in time (>20 s) and/or robust in space (>20 adjacent vertices). Depending on whether the data segment of a vertex belonged to a GC cluster, the power spectrum was marked as inside or outside cluster.

The data segments inside the clusters showed consistently less power in the 13- to 16-Hz range, but greater power in the lower (1–7 Hz) and higher ends (30–55 Hz) of the spectrum compared with those outside the cluster (Fig. 3*B*). A complete list of all of the difference scores and their significance can be found in Table S1. These results provided a spectral fingerprint for the relationship between the directed influence from the PCC to the ACC and the power changes within the ACC.

Finally, we tested whether cross-frequency coupling existed between the lower and higher ends of the spectrum. This idea stemmed from the literature showing that, during particular cognitive processing, the phase of a slow activity component (typically in the theta band) can modulate the amplitude of a fast component (typically in the gamma band) (21, 22). If this pattern existed between the theta and gamma components found in Fig. 3*B*, it would provide evidence that the spectral fingerprint was not random but carried functional information.

Following the procedure in ref. 23, we found a coupling pattern between the 3- to 4-Hz and the 30- to 55-Hz components of the ACC activity: the estimated gamma amplitude peaked around $\pm\pi/2$ of the 3- to 4-Hz phase (Fig. 3*C*). χ^2 tests confirmed the significance of this observation (Fig. 3*D*). Specifically, if there was no coupling, the phase angles corresponding to the top 5% of the gamma amplitudes would distribute evenly over the $[-\pi, \pi]$ interval. By contrast, the χ^2 test was found significant ($\chi_{99}^2 = 141.1, P < 0.01$), demonstrating deviation from a uniform distribution (Fig. 3*D*). No significant coupling was found for the other lower-frequency components in the 1- to 7-Hz band.

Discussion

We investigated the relationship between dynamic connectivity and localized neural activity in the two core regions of the DMN. Combining fcMRI and MEG, we identified spatially specific, directionally asymmetric GC influence from the PCC to the ACC in the 10-Hz range. The time-varying strength of this GC influence was associated with power alterations in the ACC: strong GC corresponded to a decrease of power around 13–16 Hz and an increase of power in the lower (1–7 Hz) and higher (30–55 Hz) ends of the spectrum. There was also significant coupling between the phase of the lower-frequency and the amplitude of the higher-frequency components in the ACC. These findings highlight an approach for studying the integration and segregation of brain activity under a unified framework, shedding light on dynamic cross-region interactions in the DMN.

Functional Connectivity and Local Neural Activity May Be Interdependent. Functional connectivity between cortical regions and localized activity within regions have been studied in separate bodies of literature (5–8). Here, we show that the two characteristics are interdependent in a real-time manner. It is worth noting that this relationship should not be interpreted as causal. It is possible that network interactions resulted in the local power fluctuation; it is also possible that changes in local dynamics affected the network coupling. The current analysis cannot disambiguate the two cases. Nonetheless, this regional activity–network interaction association may elucidate how functional specialty is preserved within regions that are coupled together.

Functional Connectivity Between PCC and ACC Is Dominated by the 10-Hz Oscillations. In previous studies, the search for neural correlates of functional connectivity in the DMN has uncovered a wide spectrum of oscillatory components, among which the alpha/low-beta frequency range was the most commonly reported (13–16, 24–27). Here, consistently, we found that the alpha oscillation is the major contributor to ACC–PCC connectivity (Fig. 1). This conclusion is not based solely on the dominant carrier frequency observed in the power correlation but also the cross-subject correlation between fcMRI and the power correlation.

The subsequent results also supported this conclusion. First, the GC analysis demonstrated that there is directed influence from the PCC to the ACC (Fig. 2*C*) beyond their power cofluctuation. Also, the ACC power–GC association in the theta and gamma bands (Fig. 3*B*) indicates that not all network-related power fluctuations contribute to the cross-region correlation. While caution must be taken using the power envelope to measure MEG connectivity (27), the cross-validating evidence here suggests that the 10-Hz oscillations are the major contributors to ACC–PCC interactions.

Directional GC Asymmetry Supports the Role of the PCC as a Network Hub. We have shown that the GC influence from the PCC to the ACC is stronger than that in the opposite direction (Fig. 2). This asymmetry is consistent with the recent finding that the information flow from posterior to anterior brain regions is mainly in the alpha/beta band (28). This asymmetry is also consistent with the role of the PCC as a structural (29) and functional (25) hub in the cortex. Especially in ref. 25, the PCC was found to transiently coordinate the interaction between resting-state networks. Here, the directional influence on the ACC may be part of the PCC's coordinating activity carried out in the DMN. If so, the associated spectral changes in the ACC may help elucidate the neurophysiological consequences of the network coordinating activity.

In the literature, theta-band activity was reported to dominate the directed information flow from anterior to posterior regions (28). We did not observe this theta dominance in the GC from the ACC to the PCC. One possibility is that the interheartbeat

segments contain too few theta cycles to reach the statistical power for GC estimation. This problem may be further explored in the future by extending the GC time periods while carefully excluding the heartbeat artifacts.

A potential concern is that the asymmetry of influence may be an artifact of different signal-to-noise ratios (SNRs) in the ACC and the PCC (30). While the exact noise level is unmeasurable, there are some observations that may alleviate this concern. First, although the occipital cortex is known to exhibit strong resting-state alpha oscillations, it did not show up as a consistent ROI in the GC maps (Fig. 2*C*). Second, although systematic SNR differences may also exist in the other frequency bands, no consistent ROI was observed in the GC maps of the other frequencies (Figs. S1 and S2). Third, while surface sources tend to have a higher SNR than deep sources in MEG, the surface GC-flow did not show systematic larger values than the deep GC-flow (Figs. S1 and S2).

The Cross-Frequency Coupling Suggests the ACC's Role in Cortical Excitability Regulation. Although both being core regions of the DMN, the ACC is functionally heterogeneous from the PCC (31). In task-based behavioral studies, the ACC has been considered a major region related to executive functions and goal-directed behavior (32, 33). Here, the phase–amplitude relationship we found between the theta and gamma frequencies is known as a neurophysiological reflection of cortical excitability (22, 34–36). It seems plausible to have an executive function-related region constantly modulated for its excitability during the resting state, so that the brain can flexibly switch from passive to active behavioral states. This has been proposed by work from a theoretical perspective (34, 37), but neurophysiological evidence remains scarce. Our finding may provide a test ground for further investigations on this hypothesis.

Insight for Future Investigation on Task Data. Simultaneous EEG–fMRI studies have reported task-introduced increases of theta/gamma power and decreases of alpha/beta power, in correspondence with the increase of BOLD activity (38). This spectral pattern seems to mirror the GC-associated power fluctuation shown in Fig. 3*B*. Given that the DMN has elevated BOLD activity in the resting state (18, 19), this spectral pattern may reveal a common neurophysiological correlate of increased BOLD activity. It may be interesting to revisit some of the task data and see whether any of the spectral changes were induced by network interactions.

Importantly, revealing brain activity during "resting state" may lead to a better understanding of brain activity during specific cognitive tasks. The highly structured resting-state dynamics indicate a nonflat "baseline" for various tasks. For example, the ACC power–GC association can be observed from the same set of subjects during episodic memory retrieval (*SI Results* and Fig. S3). The power–GC association during resting state (Fig. 3*B*) can provide critical information about how memory-related processes modulate the ongoing neural dynamics (*SI Results*).

Technical Considerations. A common concern with MEG recordings has been the low SNR often seen in deep sources (39). Here, several methodological considerations were taken to reduce the influence of noise. First, we used a multimodal imaging approach to validate functional connectivity. The fcMRI and the MEG connectivity were measured from different imaging modalities. The fact that they correlate across subjects (Fig. 1*B*) helps validate the MEG results. Second, we used a data-driven approach to identify connectivity between regions. The seed-based maps did not use preselected ROIs but still identified spatially specific connectivity between the ACC and the PCC (Fig. 2*C*). This was a cross-validation of the 10-Hz-range connectivity in Fig. 1*A*. Third, we used the interheartbeat data segments to reduce heartbeat noise and provide multiple samples of GC. Sufficient samples allowed us to create conjunction maps and examine consistency across individuals, gaining greater statistical power than using the mean values of a group result.

The choice of GC in measuring connectivity is out of the concern for "crosstalk" (10, 40). Crosstalk refers to the spurious zero-lag correlation among the source signals, an unavoidable consequence of the MEG inverse solution. In the current study, we took advantage of the fact that GC measures time-lagged interaction between sources. Moreover, taking the difference score of the to-seed and from-seed GC (i.e., GC-flow) helps cancel the artifact if crosstalk affects both directions equally. Nevertheless, we note that the zero-lag correlation can still bias the GC measure (41, 42). Crosstalk is a special case of the additive noise problem in GC measurement (42). Interested readers can refer to *Supporting Information* for a simulated demonstration of this issue (*SI Results*, Table S2, and Figs. S4 and S5). In summary, GC is affected by the level of crosstalk, but its true value can be recovered by orthogonalizing the source signals. Our GC result proved to be robust using orthogonalized ACC and PCC sources (Fig. S6). Given the lack of literature on this topic, we hope this work can bring future interest to the related research.

Finally, we note that the "hidden-node" problem (43) inherent to GC also applies here. The influence from the PCC to the ACC may go through a third region that was not captured in the GC map. Since the mapping covered all vertices in the cortex, the hidden influence, if present, would be likely coming from subcortical structures. This issue could not be resolved from the current data due to a lack of subcortical recordings.

Materials and Methods

Subjects and the Resting-State Experiment. Twenty-nine subjects (20 females; mean age, 21.4 y) were seated in the upright position, facing a screen with cross hairs shown at the center. The subjects were asked to maintain fixation on the cross hair and refrain from blinking as much as they could during the experiments. These instructions were given in both the MEG and fMRI sessions. All subjects successfully followed the instructions, and no data were discarded due to excessive blinking. This study was approved by the institutional review board at Massachusetts General Hospital, and all subjects gave signed informed consent.

Structural and Functional MRI Recordings. Anatomical images were acquired on the same day as the MEG experiment for each subject (*SI Materials and Methods*). FreeSurfer was used to reconstruct the cortical surface and downsample it to 8,192 vertices. The fMRI and MEG analyses were based on signals from the same vertices on the decimated surface. Functional recordings of the BOLD signal used the same resting-state experiment setup (*SI Materials and Methods*). Each subject's BOLD data were then coregistered to the individual's structural MRI and underwent commonly used preprocessing (*SI Materials and Methods*).

MEG Recording and Preprocessing. MEG was continuously recorded in a magnetically shielded room with a 306-channel whole-head system at a sampling rate of 1,037 Hz (*SI Materials and Methods*). All preprocessing steps used the MNE-Python toolbox (ref. 44 and *SI Materials and Methods*).

Source Estimation. The gain matrix needed for source estimation was computed using a single-compartment boundary element model (45). The source time courses were estimated using a cortically constrained minimum L_2-norm estimate (MNE) (46), with noise covariance computed from empty-room recordings on the same day. The source current density was then normalized by an estimate of projected noise to generate the dynamic statistical parametric map (dSPM) (47). The dSPM was treated as the source activity and estimated at each time point.

Definition of the ACC and PCC Regions. The regions of the ACC and PCC for the fcMRI and MEG power correlation analyses were defined according to a DMN atlas from ref. 48. The DMN atlas defines labels of the ACC and PCC on the *fsaverage* template brain surface (FreeSurfer 5.4). The labels were then morphed into each subject's native space and used as subject-specific ROIs.

Power Correlation of the MEG Source Signal and the Permutation Test. In each subject, the 5-min time courses of the ACC and PCC sources were bandpass filtered into 55 narrow bands of 1-Hz width, which evenly divided up the 1- to 56-Hz interval. The filtered signals from each vertex of the ACC were paired up with those from each vertex of the PCC. For each pair, a phase-orthogonalized power envelope correlation was calculated using the method in ref. 15. Envelope correlations were obtained for all 55 × 55 frequency combinations, and vertex pairs of the same frequency combination were averaged together, resulting in a 55 × 55 connectivity spectrogram for each subject.

To test the robustness of the envelope correlation, the temporal order of the envelopes was permuted 1,000 times, and a connectivity spectrogram was calculated for each cohort of permuted samples. For each frequency pair, the veridical correlation was considered significant if its value exceeded the 95% quantile of the 1,000 permutated correlation scores.

fMRI-Based Connectivity. Pearson's correlation was calculated between the BOLD time series for each ACC–PCC vertex pair, and then averaged across vertex pairs to generate one fcMRI score for each subject.

Seed-Based MEG GC Maps. Heartbeat events were removed from the preprocessed signal (*SI Materials and Methods*), resulting in ∼300 short segments of MEG data in each subject. GC maps were computed for each interheartbeat segment between a seed chosen from the ACC/PCC and the rest of the cortex. Five different seeds were used for each region, and the results were averaged across the five runs. The seeds surrounded the center of the ACC and PCC labels defined by the DMN atlas. Each seed was a cortical region with a diameter of 1 cm.

For each time segment, source activities within the seed region were averaged across vertices to yield the seed time series X_t. The seed was paired with all vertices in the other region (denoted Y_t), and a bivariate autoregressive (AR) model was fitted to each pair:

$$X_t = \sum_{k=1}^{p} a_{11,k} X_{t-k} + \sum_{k=1}^{p} a_{12,k} Y_{t-k} + E_{1t}, \quad [1a]$$

$$Y_t = \sum_{k=1}^{p} a_{21,k} X_{t-k} + \sum_{k=1}^{p} a_{22,k} Y_{t-k} + E_{2t}. \quad [1b]$$

The ensemble mean of X_t and Y_t were removed beforehand. Here, p denotes the model order, $a_{ij,k}$ with $i, j \in \{1,2\}$ and $k = 1, 2, \ldots, p$ are model coefficients, and E_{1t} and E_{2t} are uncorrelated white noise. The model was fitted using the Levinson–Wiggins–Robinson algorithm with a fixed model order $P = 8$ for each vertex pair (*SI Materials and Methods* and Figs. S7 and S8).

Based on the fitted model coefficients, Geweke's frequency-domain GC (49) was estimated in the range of 2–45 Hz with a resolution of 1.5 Hz. Values in the 8- to 12-Hz interval were summed to yield the alpha-band GC. The model fitting and GC computation were done using the Python toolbox *nitime*, which follows closely the procedure described by ref. 50.

Nonparametric Cluster-Level Significance Test for Defining ROIs. For each pair of the seed–target vertex combinations, a GC difference was calculated for each interheartbeat segment, and a t score was used to summarize the difference over segments, which quantified the overall asymmetry of the influences between the seed and the target vertex. The significance of the t scores was determined by a nonparametric cluster-level test (51), which corrected for the family-wise error through a Monte-Carlo permutation that took into account the spatial correlation of nearby vertices. Test statistics with a P value lower than 0.05 were considered significant. The test was carried out in each subject's native space, and the results were morphed into the *fsaverage* space for group average and conjunction analysis.

Spatiotemporal Clustering of the GC Values. Spatiotemporal clusters of alpha-band GC values over adjacent vertices and time segments were identified. A threshold was set to two times the interquartile distance above the median across all vertices and time segments. Above-threshold GC values from more than 20 adjacent vertices and/or time segments were marked as spatiotemporal clusters. The number 20 was chosen so that the marked clusters were extensive enough in space (20 vertices covered an area ≈2 cm in diameter) or lasted long enough in time (20 time segments covered ≈20 s), which indicated robust GC influence that was unlikely driven by transient random fluctuations of noise in the signal.

Comparison of Power Inside and Outside the GC Clusters. The PSD of the vertices and time segments inside the spatiotemporal clusters were compared with those outside the clusters. The test followed ref. 52. Briefly, the PSD $S(f)$ was averaged across vertices and time segments and transformed to obtain Gaussianity:

$$x(f) = \log[S(f)] - \psi(m) + \ln(m), \quad [2]$$

where m equals one-half the number of Slepian sequences multiplied by the number of samples, and ψ is the digamma function. Once the mean power spectra $x_1(f)$ and $x_2(f)$ of two different groups were computed, the PSD-difference score was calculated as follows:

$$\Delta x(f) = \frac{x_1(f) - x_2(f)}{\sqrt{\psi'(m_1) + \psi'(m_2)}}, \quad [3]$$

where m_1 and m_2 are the number of samples averaged in $x_1(f)$ and $x_2(f)$, and ψ' is the trigamma function. $\Delta x(f)$ assimilates the statistic of a paired t test in representing the difference between $x_1(f)$ and $x_2(f)$.

Estimation of the Cross-Frequency Phase–Amplitude Coupling. The entire time course (5 min) of the source activity of each seed was filtered into six narrow-band lower-frequency components (1–2, 2–3, 3–4, 4–5, 5–6, and 6–7 Hz). The phase angle at each time point was obtained via Hilbert transform. The amplitudes of the gamma band (30–55 Hz) from the same signal were extracted across the same time points. Thus, the lower-frequency phase and gamma-frequency amplitude were paired across time. The coupling was estimated following a spline-fitting procedure (23). Briefly, the gamma amplitude was modeled as a function of the lower-frequency phase over 100 equally spaced phase bins dividing the $[-\pi, \pi]$ interval. The function was fitted with cardinal spline basis using 20 control points that evenly divided the phase interval. The estimated function represents the distribution of gamma amplitudes over $[-\pi, \pi]$.

ACKNOWLEDGMENTS. We thank Dr. Kyle Lepage for his advice on the power spectral analysis and Dr. Martin Luessi for his help with MEG preprocessing. This work was supported by the Cognitive Rhythms Collaborative Grant (NSF-DMS-1042134) and jointly with NIH Grants R01NS091604, P50MH106435, R01NS0699696, P41EB015896, S10RR014978, R01NS095369, and MH099765 and Beijing Municipal Science and Technology Commission Z161100002616009.

1. Mesulam MM (1990) Large-scale neurocognitive networks and distributed processing for attention, language, and memory. *Ann Neurol* 28:597–613.
2. Tononi G, Edelman GM (1998) Consciousness and complexity. *Science* 282:1846–1851.
3. Sporns O (2010) *Networks of the Brain* (MIT Press, Cambridge, MA).
4. Bressler SL, Menon V (2010) Large-scale brain networks in cognition: Emerging methods and principles. *Trends Cogn Sci* 14:277–290.
5. Baillet S, Mosher JC, Leahy RM (2001) Electromagnetic brain mapping. *IEEE Signal Process Mag* 18:14–30.
6. Poldrack RA (2007) Region of interest analysis for fMRI. *Soc Cogn Affect Neurosci* 2: 67–70.
7. Biswal B, Yetkin FZ, Haughton VM, Hyde JS (1995) Functional connectivity in the motor cortex of resting human brain using echo-planar MRI. *Magn Reson Med* 34:537–541.
8. Friston KJ (2011) Functional and effective connectivity: A review. *Brain Connect* 1:13–36.
9. Logothetis NK (2008) What we can do and what we cannot do with fMRI. *Nature* 453: 869–878.
10. Brookes MJ, et al. (2011) Measuring functional connectivity using MEG: Methodology and comparison with fcMRI. *Neuroimage* 56:1082–1104.
11. Hutchison RM, et al. (2013) Dynamic functional connectivity: Promise, issues, and interpretations. *Neuroimage* 80:360–378.
12. Laumann TO, et al. (September 2, 2016) On the stability of BOLD fMRI correlations. *Cereb Cortex*, 10.1093/cercor/bhw265.
13. de Pasquale F, et al. (2010) Temporal dynamics of spontaneous MEG activity in brain networks. *Proc Natl Acad Sci USA* 107:6040–6045.
14. Brookes MJ, et al. (2011) Investigating the electrophysiological basis of resting state networks using magnetoencephalography. *Proc Natl Acad Sci USA* 108: 16783–16788.
15. Hipp JF, Hawellek DJ, Corbetta M, Siegel M, Engel AK (2012) Large-scale cortical correlation structure of spontaneous oscillatory activity. *Nat Neurosci* 15:884–890.
16. Marzetti L, et al. (2013) Frequency specific interactions of MEG resting state activity within and across brain networks as revealed by the multivariate interaction measure. *Neuroimage* 79:172–183.
17. Baker AP, et al. (2014) Fast transient networks in spontaneous human brain activity. *eLife* 3:e01867.
18. Shulman GL, et al. (1997) Common blood flow changes across visual tasks: II. Decreases in cerebral cortex. *J Cogn Neurosci* 9:648–663.
19. Raichle ME, et al. (2001) A default mode of brain function. *Proc Natl Acad Sci USA* 98: 676–682.

20. Buckner RL, Andrews-Hanna JR, Schacter DL (2008) The brain's default network: Anatomy, function, and relevance to disease. *Ann N Y Acad Sci* 1124:1–38.
21. Schröeder CE, Lakatos P (2009) Low-frequency neuronal oscillations as instruments of sensory selection. *Trends Neurosci* 32:9–18.
22. Canolty RT, Knight RT (2010) The functional role of cross-frequency coupling. *Trends Cogn Sci* 14:506–515.
23. Kramer MA, Eden UT (2013) Assessment of cross-frequency coupling with confidence using generalized linear models. *J Neurosci Methods* 220:64–74.
24. Mantini D, Perrucci MG, Del Gratta C, Romani GL, Corbetta M (2007) Electrophysiological signatures of resting state networks in the human brain. *Proc Natl Acad Sci USA* 104:13170–13175.
25. de Pasquale F, et al. (2012) A cortical core for dynamic integration of functional networks in the resting human brain. *Neuron* 74:753–764.
26. Jerbi K, et al. (2010) Exploring the electrophysiological correlates of the default-mode network with intracerebral EEG. *Front Syst Neurosci* 4:27.
27. Foster BL, et al. (2016) Spontaneous neural dynamics and multi-scale network organization. *Front Syst Neurosci* 10:7.
28. Hillebrand A, et al. (2016) Direction of information flow in large-scale resting-state networks is frequency-dependent. *Proc Natl Acad Sci USA* 113:3867–3872.
29. Hagmann P, et al. (2008) Mapping the structural core of human cerebral cortex. *PLoS Biol* 6:e159.
30. Newbold P (1978) Feedback induced by measurement errors. *Int Econ Rev* 19:787–791.
31. Vogt BA, Finch DM, Olson CR (1992) Functional heterogeneity in cingulate cortex: The anterior executive and posterior evaluative regions. *Cereb Cortex* 2:435–443.
32. Bush G, Luu P, Posner MI (2000) Cognitive and emotional influences in anterior cingulate cortex. *Trends Cogn Sci* 4:215–222.
33. Carter CS, et al. (1998) Anterior cingulate cortex, error detection, and the online monitoring of performance. *Science* 280:747–749.
34. He BJ, Raichle ME (2009) The fMRI signal, slow cortical potential and consciousness. *Trends Cogn Sci* 13:302–309.
35. Lisman JE, Jensen O (2013) The theta-gamma neural code. *Neuron* 77:1002–1016.
36. Hyafil A, Giraud AL, Fontolan L, Gutkin B (2015) Neural cross-frequency coupling: Connecting architectures, mechanisms, and functions. *Trends Neurosci* 38:725–740.
37. Deco G, Jirsa VK, McIntosh AR (2011) Emerging concepts for the dynamical organization of resting-state activity in the brain. *Nat Rev Neurosci* 12:43–56.
38. Scheeringa R, et al. (2011) Neuronal dynamics underlying high- and low-frequency EEG oscillations contribute independently to the human BOLD signal. *Neuron* 69: 572–583.
39. Hillebrand A, Barnes GR (2002) A quantitative assessment of the sensitivity of whole-head MEG to activity in the adult human cortex. *Neuroimage* 16:638–650.
40. Schoffelen JM, Gross J (2009) Source connectivity analysis with MEG and EEG. *Hum Brain Mapp* 30:1857–1865.
41. Nolte G, et al. (2008) Robustly estimating the flow direction of information in complex physical systems. *Phys Rev Lett* 100:234101.
42. Vinck M, et al. (2015) How to detect the Granger-causal flow direction in the presence of additive noise? *Neuroimage* 108:301–318.
43. Pearl J (2009) *Causality* (Cambridge Univ Press, Cambridge, UK).
44. Gramfort A, et al. (2014) MNE software for processing MEG and EEG data. *Neuroimage* 86:446–460.
45. Hämäläinen MS, Sarvas J (1987) Feasibility of the homogeneous head model in the interpretation of neuromagnetic fields. *Phys Med Biol* 32:91–97.
46. Hämäläinen MS, Ilmoniemi RJ (1994) Interpreting magnetic fields of the brain: Minimum norm estimates. *Med Biol Eng Comput* 32:35–42.
47. Dale AM, et al. (2000) Dynamic statistical parametric mapping: Combining fMRI and MEG for high-resolution imaging of cortical activity. *Neuron* 26:55–67.
48. Yeo BT, et al. (2011) The organization of the human cerebral cortex estimated by intrinsic functional connectivity. *J Neurophysiol* 106:1125–1165.
49. Geweke J (1982) Measurement of linear dependence and feedback between multiple time series. *J Am Stat Assoc* 77:304–313.
50. Ding M, Chen Y, Bressler SL (2006) Granger causality: Basic theory and application to neuroscience. *Handbook of Time Series Analysis*, eds Schelter B, Winterhalder M, Timmer J (Wiley, Hoboken, NJ), pp 437–460.
51. Maris E, Oostenveld R (2007) Nonparametric statistical testing of EEG- and MEG-data. *J Neurosci Methods* 164:177–190.
52. Bokil H, Purpura K, Schoffelen J-M, Thomson D, Mitra P (2007) Comparing spectra and coherences for groups of unequal size. *J Neurosci Methods* 159:337–345.
53. O'Neill GC, et al. (2015) Dynamic recruitment of resting state sub-networks. *Neuroimage* 115:85–95.
54. Chatfield C (2003) *The Analysis of Time Series* (CRC Press, Boca Raton, FL), p 64.
55. Akaike H (1973) Information theory as an extension of the maximum likelihood principle. *Second International Symposium on Information Theory* (Akademiai Kiado, Budapest), pp 267–281.
56. Pardey J, Roberts S, Tarassenko L (1996) A review of parametric modelling techniques for EEG analysis. *Med Eng Phys* 18:2–11.